

Dynamics of interacting dark soliton stripes

P G Kevrekidis, Wenlong Wang, Georgios Theocharis, Dimitris Frantzeskakis, R Carretero-González, B P Anderson

▶ **To cite this version:**

P G Kevrekidis, Wenlong Wang, Georgios Theocharis, Dimitris Frantzeskakis, R Carretero-González, et al.. Dynamics of interacting dark soliton stripes. Physical Review A, 2019, 100, 10.1103/PhysRevA.100.033607 . hal-02371084

HAL Id: hal-02371084
https://hal.science/hal-02371084

Submitted on 19 Nov 2019

HAL is a multi-disciplinary open access archive for the deposit and dissemination of scientific research documents, whether they are published or not. The documents may come from teaching and research institutions in France or abroad, or from public or private research centers.

L'archive ouverte pluridisciplinaire **HAL**, est destinée au dépôt et à la diffusion de documents scientifiques de niveau recherche, publiés ou non, émanant des établissements d'enseignement et de recherche français ou étrangers, des laboratoires publics ou privés.

Dynamics of interacting dark soliton stripes

P. G. Kevrekidis,[1,*] Wenlong Wang,[2,†] G. Theocharis,[3] D. J. Frantzeskakis,[4] R. Carretero-González,[5] and B. P. Anderson[6]

[1]*Department of Mathematics and Statistics, University of Massachusetts, Amherst, Massachusetts 01003-4515, USA*

[2]*Department of Theoretical Physics, Royal Institute of Technology, Stockholm SE-106 91, Sweden*

[3]*Laboratoire d'Acoustique de l'Université du Maine, UMR-CNRS 6613, Avenue Olivier Messiaen, Le Mans 72000, France*

[4]*Department of Physics, National and Kapodistrian University of Athens, Panepistimiopolis, Zografos, 15784 Athens, Greece*

[5]*Nonlinear Dynamical Systems Group,[‡] Computational Sciences Research Center, and Department of Mathematics and Statistics, San Diego State University, San Diego, California 92182-7720, USA*

[6]*College of Optical Sciences, University of Arizona, Tucson, Arizona 85721, USA*

(Received 18 March 2019; published 9 September 2019)

In the present work we examine the statics and dynamics of multiple parallel dark soliton stripes in a two-dimensional Bose-Einstein condensate. Our principal goal is to study the effect of the interaction between the stripes on the transverse instability of the individual stripes. The cases of two-, three-, and four-stripe states are studied in detail. We use a recently developed adiabatic invariant formulation to derive a quasianalytical prediction for the stripe equilibrium position and for the Bogoliubov–de Gennes spectrum of excitations of stationary stripes. We subsequently test our predictions against numerical simulations of the full two-dimensional Gross-Pitaevskii equation. We find that the number of unstable eigenmodes increases as the number of stripes increases due to (unstable) relative motions between the stripes. Their corresponding growth rates do not significantly change, although for large chemical potentials, the larger the stripe number, the larger the maximal instability growth rate. The instability induced dynamics of multiple stripe states and their decay into vortices are also investigated.

DOI: 10.1103/PhysRevA.100.033607

I. INTRODUCTION

The study of dark solitons has attracted considerable theoretical and experimental attention in various branches of physics. Prominent examples include nonlinear optics [1] and atomic Bose-Einstein condensates (BECs) [2,3], but also mechanical [4] and electrical [5] dynamical lattices, magnetic films [6], electromagnetic [7] and acoustic [8] metamaterials, hydrodynamics [9], plasmas [10], nematic liquid crystals [11], as well as other nonlocal media [12], dipolar atomic condensates [13], and exciton-polariton condensates [14].

In the context of BECs, a number of experiments have addressed diverse phenomena including the formation of dark solitons by laser beams dragged through an elongated BEC [15], their oscillations in the trap [16,17], their pairwise interactions [17,18], as well as their transverse instability in higher-dimensional settings and their concomitant decay into vortices and vortex rings [19–22] (see the recent volume [3] summarizing many of these phenomena). Furthermore, a sizable literature has emerged in the topic of multicomponent condensates, where one of the components assumes the form of a dark soliton (see, e.g., the recent review [23] and references therein). Regarding applications, matter-wave dark solitons have been proposed for use in atomic matter-wave interferometers [24] and as qubits in BECs [25].

Generally, dark solitons are unstable against decay when embedded in a higher dimensional space. The study of their transverse (or "snaking") instability has been of particular significance since its theoretical inception [26] (see also the review [27] and references therein). However, the instabilities associated with the mutual interactions between multiple dark solitons in a BEC have been only partly investigated; see, e.g., Ref. [18] for the quasi-one-dimensional setting, as well as the recent work [28] for two- and three-dimensional settings. Importantly, these works always considered the role of trap induced confinement in the corresponding dimensionality of the problem. In the higher-dimensional cases, examples of stability have been reported numerically for suitable parametric regimes suppressing the snaking instability.

In the present work, we analytically and numerically characterize the dynamics of up to four parallel dark solitons, finding that while the number of unstable eigenmodes increases as the number of stripes increases, their corresponding growth rates do not significantly change; nevertheless for large chemical potentials the rates are found to increase with the stripe number. Progress on this front is especially relevant in experimental settings that involve solitons produced in the merging or collisions of BECs [29], the interaction of multiple dark solitons [17,18,20,21], or the decay of multiple dark solitons as a generator of vortices [19] and two-dimensional (2D) quantum turbulence [30] in BECs as well as in optics [31]. The subject of dark soliton decay also continues to attract theoretical attention [32,33], including the possibility of "engineering" avoidance of this instability [34].

*kevrekid@math.umass.edu
†wenlongcmp@gmail.com
‡http://nlds.sdsu.edu.

 ©2019 American Physical Society

In recent work [35,36], we provided a framework for addressing the transverse instability of a diverse array of structures including dark soliton stripes, ring dark solitons (extensively studied in optics [37–39] and BECs [40–43]), and spherical shell solitons [37,44–46], as well as dark-bright solitons in multicomponent BECs [23]. Our approach in the present work involves extending this formulation to the case of multisoliton settings. We seek to understand how the presence of a secondary stripe may affect the growth rate of a transverse instability. To address this problem we combine the adiabatic invariant (AI) of a single dark soliton stripe [36] with the pairwise interaction between the stripes. This allows us to identify the equilibrium states of the multiple stripes, and more importantly the modes of linearization as per the well established Bogolyubov–de Gennes (BdG) analysis, around the solitonic multistripe solution. Finally, this formulation enables an exploration of the fully nonlinear stage of the instability by examining the filament partial differential equation (PDE) for each of the relevant stripes. While the analytical framework becomes rather complex as the number of stripes increases, we explore the relevant instability numerically for larger stripe numbers (such as 3 and 4).

Our presentation is structured as follows. In Sec. II we provide the theoretical analysis of the case of two dark soliton stripes, which we refer to as "two stripes." In Sec. III, we explore numerically the scenarios of two, three, and four stripes and, where appropriate, compare with the semianalytical predictions of the filament theory. Finally, in Sec. IV, we summarize our findings and present our conclusions, as well as a number of directions for future work.

II. THEORETICAL ANALYSIS

The model under consideration is the normalized 2D Gross-Pitaevskii equation (GPE), describing a condensate confined in a highly oblate trap along the z axis of frequency ω_z [3]:

$$iu_t = -\tfrac{1}{2}(u_{xx} + u_{yy}) + |u|^2 u + V(x)u, \tag{1}$$

where subscripts denote partial derivatives and $u(x, y, t)$ denotes the wave function. Here, the density $|u|^2$, length, time, and energy are respectively measured in units of $2\sqrt{2\pi}aa_z$, a_z, ω_z^{-1}, and $\hbar\omega_z$, where a and a_z are, respectively, the s-wave scattering length and harmonic oscillator length in the z direction. The external potential is given by

$$V(x) = \tfrac{1}{2}\Omega^2 x^2, \tag{2}$$

which is independent of the transverse y direction, with $\Omega = \omega_x/\omega_z$ being the trap's aspect ratio. After this dimension reduction, we carry out a subsequent scaling and consider $\Omega = 1$ (see Sec. III A for more details).

The model is supplemented with periodic boundary conditions in the y direction. Equation (1), for $V = 0$, conserves the Hamiltonian

$$H = \frac{1}{2}\iint_{-\infty}^{\infty} [|u_x|^2 + |u_y|^2 + (|u|^2 - \mu)^2]dx\,dy, \tag{3}$$

where μ is the chemical potential. In the dimensionless form of the GPE given here, we consider chemical potentials ranging from the linear limit up to $\mu = 80$ in the Thomas-Fermi limit. This range is sufficient to address the chemical potential and atomic densities in typical experimental BECs; see Ref. [3] for a detailed discussion on the translation between dimensionless and dimensional units.

Let us first study the case of two dark soliton stripes. To describe each stripe, we consider the following ansatz:

$$u = e^{-i\mu t}[\sqrt{\mu - v^2}\tanh(\sqrt{\mu - v^2}(x - x_0)) + iv], \tag{4}$$

which is the functional form of the quasi-one-dimensional dark soliton solution of Eq. (1), for $V = 0$, that extends uniformly in the y direction. In the 2D setting under consideration, Eq. (4) describes a one-dimensional dark soliton stripe embedded in 2D space, characterized by its center x_0 and velocity $v = x_{0t} \equiv dx_0/dt$. In order to describe the transverse instability-induced undulation of the stripe, we assume that the center position x_0 is not solely a function of t, but also a function of the transverse variable y, i.e., $x_0 = x_0(y, t)$. We also wish to consider cases in which the potential $V(x)$ may be nonzero, which involves replacing μ with $\mu - V(x_0)$ (representing the effective, or *local*, chemical potential where the dark soliton is sitting) in Eqs. (4) and (3). Then, substituting the ansatz (4) into the Hamiltonian (3), we obtain the following "effective energy" (an adiabatic invariant) of the stripe:

$$E = \frac{4}{3}\int_{-\infty}^{\infty}\left(1 + \frac{1}{2}x_{0y}^2\right)\left(\mu - V(x_0) - x_{0t}^2\right)^{3/2}dy. \tag{5}$$

Here, the transverse energy contribution (of the $|u_y|^2$ term) has been accounted for through the term proportional to x_{0y}^2. For convenience, hereafter we use the following compact notation:

$$A = \mu - V(x_0) - x_{0t}^2, \quad B = 1 + \frac{1}{2}x_{0y}^2.$$

Earlier work on the interaction of dark solitons [47,48] in one-dimensional (1D) settings, including relevant work in the context of quasi-1D atomic BECs [17,18,49], has quantified the interaction effect between dark solitons. Now, this interaction becomes a pointwise effect across the stripes, when the interaction term is integrated along x, as per the variational formulation of Ref. [48]. Thus the corresponding energy, incorporated through its last term this interaction effect, reads

$$E = 2\int_{-\infty}^{\infty}\left(\frac{4}{3}A^{3/2}B - 8A^{3/2}e^{-4A^{1/2}x_0}\right)dy.$$

Here, we have used the symmetry of the two solitons, which are assumed to be located at $\pm x_0(y)$. This represents the simplest possible scenario, where a single dynamical variable, x_0 (i.e., the symmetric position of the two solitons), can adequately describe the dynamics of both. Nevertheless, it should be pointed out that this scenario is of direct relevance to experiments [17,18]. Due to the consideration of two solitons, the energy of each individual soliton is doubled, hence the factor of 2 in front of the integral.

We can now find the evolution of the two-stripe parameter x_0 from energy conservation, $dE/dt = 0$. Indeed, the relevant

calculation leads to the following PDE for x_0:

$$B\left(x_{0tt}+\frac{V'}{2}\right)+\frac{A}{3}x_{0yy} = \frac{V'}{2}x_{0y}^2+x_{0y}x_{0t}x_{0ty} - [(V'+2x_{0tt})(-3+4A^{1/2}x_0)-8A^{3/2}]e^{-4A^{1/2}x_0}, \quad (6)$$

where $V' \equiv \partial V/\partial x_0$. Hereafter, the above equation will be called the "adiabatic invariant PDE" (AI PDE).

The next step is to examine the stationary states of this PDE and their stability. As we know, there exists a homogeneous (independent of y) solution corresponding to the two parallel soliton stripes. Retrieving that, as well as its linearization, yields information about the existence and stability of the two-stripe state, and more specifically on how the presence of a second stripe affects the transverse (in)stability of the first one.

More specifically, we seek a symmetric pair of soliton stripes with x_0 independent of y that yields the following algebraic (transcendental) equation for x_0 (see, e.g., Ref. [18] for a relevant analysis):

$$-\frac{V'}{2}=e^{-4A_0^{1/2}x_0}\left[V'\left(-3+4A_0^{1/2}x_0\right)-8A_0^{3/2}\right], \quad (7)$$

where $A_0=\mu-V(x_0)$. Notice that results stemming from Eq. (7) are expected to be more accurate in the framework of the so-called particle approximation, whereby individual solitons feature a particle-like nature; this situation corresponds to the case of sufficiently large values of the chemical potential μ, the so-called Thomas-Fermi (TF) large density limit. Thus, this step leads to the determination of the equilibrium positions $\pm x_0^{(\mathrm{eq})}$ of the constituent stripe solitons forming the stationary stripe pair. Then, the stability of $x_0^{(\mathrm{eq})}$ can be studied by introducing the ansatz

$$x_0=x_0^{(\mathrm{eq})}+\epsilon X_1(t)\cos(k_n y),$$

with $k_n=n\pi/L_y$ denoting the transverse perturbation wave numbers and L_y being half the size of the computational domain in the y direction; see below. Then, we linearize with respect to the small-amplitude perturbation $X_1(t)$, and determine whether such a stationary stripe pair is robust under transverse modulations or not. By doing so, we obtain a rather elaborate expression that can be summarized as

$$RX_{1tt}=-\left[\tfrac{1}{2}V''(x_0)-\tfrac{1}{3}k_n^2A_0+S\right]X_1.$$

Here, $A_0=A(t=0)$ and the coefficients R and S are given by

$$R=1+2\left(-3+4A_0^{1/2}x_0\right)e^{-4A_0^{1/2}x_0},$$
$$S=R\left[-4S_1\left(V'(x_0)S_2-8A_0^{3/2}\right)+4V'(x_0)S_1\right] +\left[V''(x_0)S_2+12V'(x_0)A_0^{1/2}\right]R_0,$$

where $S_0=e^{-4A_0^{1/2}x_0}$, $S_1=A_0^{1/2}-V'A_0^{-1/2}x_0/2$, and $S_2=-3+4A_0^{1/2}x_0$. Note that here, for simplicity, we have used x_0 instead of $x_0^{(\mathrm{eq})}$; furthermore, both R and S are evaluated at the equilibrium position $x_0=x_0^{(\mathrm{eq})}$. With the equation of motion for a generic perturbation X_1, we can look for normal mode frequencies by setting

$$X_1(t)=X_1^{(0)}\exp(\lambda t),$$

where $X_1^{(0)}$ is a constant amplitude and λ is the eigenvalue of the normal mode n.

In the numerical section below, we compare this prediction about multistripe stability with detailed computations of the spectrum at the 2D GPE level. This is done upon performing the standard Bogoliubov–de Gennes (BdG) analysis (see details, e.g., in Ref. [3]). Moreover, given the favorable comparison reflected in our results, it is relevant to examine the full AI PDE dynamics of Eq. (6) against the corresponding 2D dynamical evolution of the GPE. This will help us to build a systematic appreciation of the role of soliton interactions in enhancing or mitigating transverse instabilities. It will also serve as a stepping stone towards generalizing this to a larger number of stripes, by means of the (AI PDE) extension of the significantly simpler, ODE-based, 1D picture of Refs. [18,49].

III. NUMERICAL RESULTS

A. Preliminaries

It is worth noting that the theoretical analysis in the last section applies to a generic potential $V(x)$ varying slowly on the soliton scale. In what follows, we focus on the experimentally relevant harmonic trap described by Eq. (2). For all of the numerical computations we set the trap strength $\Omega=1$. However, it is important to mention that, after a scaling transformation, smaller values for Ω would correspond to larger values of the chemical potential μ. Specifically, by defining the rescaled variables $(\bar{x},\bar{y})=\bar{\Omega}^{-1/2}(x,y)$, $\bar{u}=\bar{\Omega}^{1/2}u$, and $\bar{\mu}=\bar{\Omega}\mu$, Eq. (1) with $\Omega=1$ transforms to the same equation but with arbitrary $\bar{\Omega}$.

As for our computational domain we use $(x,y)\in[-L_x,L_x]\times[-L_y,L_y]$ with periodic boundary conditions in y. The values of L_x and L_y will be chosen as $L_x=16$ and $L_y=2$, $L_y=4$, or $L_y=8$. In terms of physical parameters, and for $L_y=4$, one may estimate the system parameters corresponding to a ^{87}Rb condensate confined in a parabolic trap with $\omega_z=2\pi\times100$ Hz. In this case, the number of atoms (resulting from the normalization of the wave function) is given by

$$N=\frac{4L_y}{3\sqrt{\pi}}\left(\frac{a_z}{a}\right)\mu^{3/2}.$$

For ^{87}Rb, the s-wave scattering length is $a=5.3$ nm. The trapping frequency ω_z corresponds to a harmonic oscillator length $a_z=\sqrt{\hbar/(m\omega_z)}=2.7\ \mu$m. With these parameters, typical numbers of atoms, as well as respective values of the healing length $\xi=\hbar/\sqrt{2mg_{2D}n_{2D}}$ (where $g_{2D}=2\sqrt{2\pi}aa_z\hbar\omega_z$ is the effective 2D interaction strength and n_{2D} the peak density [3]), are as follows: for a (dimensionless) chemical potential $\mu=1$, one has $N\sim1500$ atoms and $\xi\sim1.9\ \mu$m; for $\mu=40$ the respective values are $N\sim3.9\times10^5$ atoms and $\xi\sim0.3\ \mu$m; while for $\mu=80$, we have $N\sim10^6$ atoms and $\xi\sim0.2\ \mu$m. Notice that the above characteristic values of the chemical potential correspond to various numerical results that will be presented below. Furthermore, in the simulations depicting stripe dynamics, the time unit $t=1$ corresponds to $\sim$2 ms.

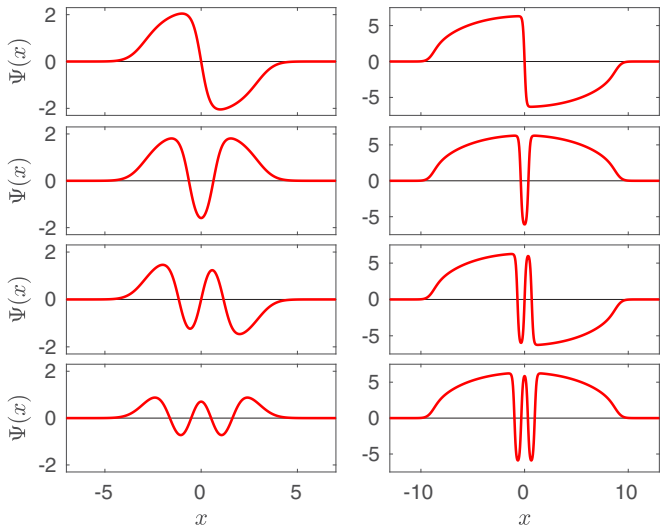


FIG. 1. Cross sections ($y = \text{const}$) along the x direction of typical wave functions Ψ [which are found from the GPE (1) using $u(x, y, t) = \Psi(x)\exp(-i\mu t)$] corresponding from top to bottom to one, two, three, and four dark solitons, respectively. In all cases $\Omega = 1$ and $\mu = 5$ (left) and $\mu = 40$ (right) correspond to chemical potential values close to the linear (small density) and Thomas-Fermi (large density) limits, respectively. Note that these 2D stationary states are homogeneous in the y direction, as the potential (2) is only x dependent. All quantities in this and subsequent figures are dimensionless; see text.

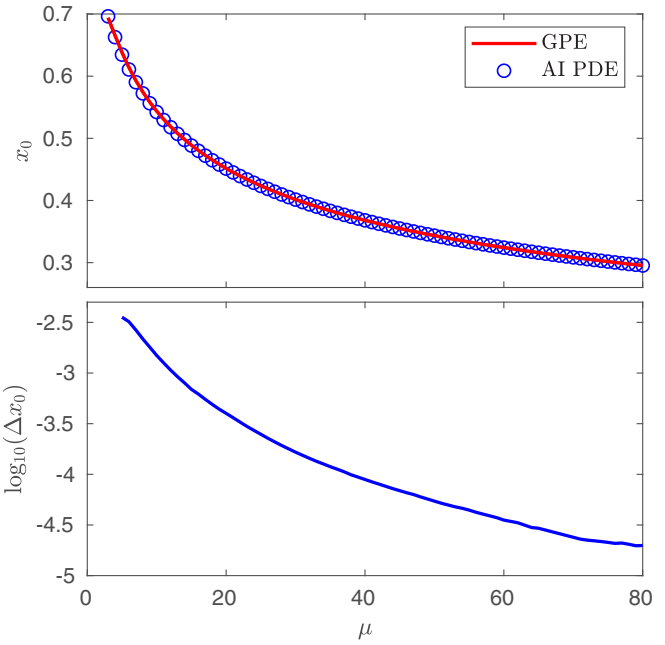


FIG. 2. Top: Equilibrium position $x_0 = x_0^{(\text{eq})}$ for the two-stripe case, as obtained from the GPE (1) (red line) and the AI PDE model (6) (blue circles). Bottom: Difference Δx_0 between the equilibrium position from the GPE (1) and the one predicted by the AI PDE model (6). Notice the remarkably good agreement even near the linear limit.

With respect to our numerical simulations, we use a computational framework, similar to our earlier works [35,36,45]. This is based on finite differences to approximate partial derivatives and the partial wave method to reconstruct the spectrum for the full (2D) system by computing a handful of 1D (x) spectra. To fully resolve the 1D spectra we used 64 000 mesh points over the interval $-16 \leqslant x \leqslant 16$.

B. Two dark soliton stripes

In the linear, low-density limit of Eq. (1), each of the dark soliton multistripe states corresponds to an eigenstate of the simple harmonic oscillator. That is, at chemical potential $\mu = (n + 1/2)\Omega$, the nth harmonic oscillator eigenfunction is a starting point for the continuation of a nonlinear state with n stripes (see, e.g., Ref. [50]). We thus use parametric continuation towards higher values of the chemical potential, gradually tending to the large chemical potential limit. In Fig. 1 we depict the different steady states with one to four stripes for the small and large density limits. It is important to stress that it is in the Thomas-Fermi (large density) limit that we expect the above developed theory to be valid. This is because, in that limit, the dark-soliton stripe width $\propto \mu^{-1/2}$ tends to 0, thus justifying its consideration as a filament (without internal dynamics).

We start with the equilibrium points of the (homogeneous) stationary stripes. Here, the comparison of the analytical prediction of Eq. (7) with the full numerical results of the GPE is depicted in Fig. 2. A remarkably good agreement is found between the two, for all of the considered values of the chemical potential, with the result indeed becoming essentially exact for sufficiently large values of μ (five digits of precision for $\mu \approx 80$). In some sense, however, this agreement should be expected, given the corresponding 1D results of Ref. [49], as well as the effectively quasi-1D nature of the pertinent equilibria. A far more challenging test of the theory lies in the examination of the corresponding linearized modes.

Once we have identified the steady states for N dark soliton stripes, we proceed to compare their respective spectra of the BdG analysis of the GPE ("BdG-GPE" hereafter) with the corresponding predictions of the AI PDE, Eq. (6). At this point, it should be recalled that, for mathematical simplicity, we have restricted consideration to two dark soliton stripes symmetrically placed around the center of the trap (in line with, e.g., the experiments of Refs. [17,18]). Therefore, the AI theory will naturally capture only the normal modes corresponding to dark soliton stripes oscillating *out of phase* (OOP); for simplicity these modes will be referred hereafter to as OOP modes. Figure 3 depicts the spectra obtained via BdG-GPE [(red and blue) dots] and AI PDE [thick (pink and orange) curves] for the two-stripe steady state. It is relevant to mention that the spectra have a strong dependence on the numerical domain, namely $(x, y) \in [-L_x, L_x] \times [-L_y, L_y]$, and particularly on the size of L_y. Specifically, since the snaking instability of dark soliton stripes is only present for relatively small wave numbers, reducing the length of the domain in the y direction results in long wavelengths being suppressed (i.e., not accessible) on this smaller domain. As a result, as L_y is reduced, more (long-wave) modes are suppressed and only shorter wavelength eigenmodes will be unstable (cf. the $L_y = 2$ and the $L_y = 4$ spectra in Fig. 3). In fact, for small

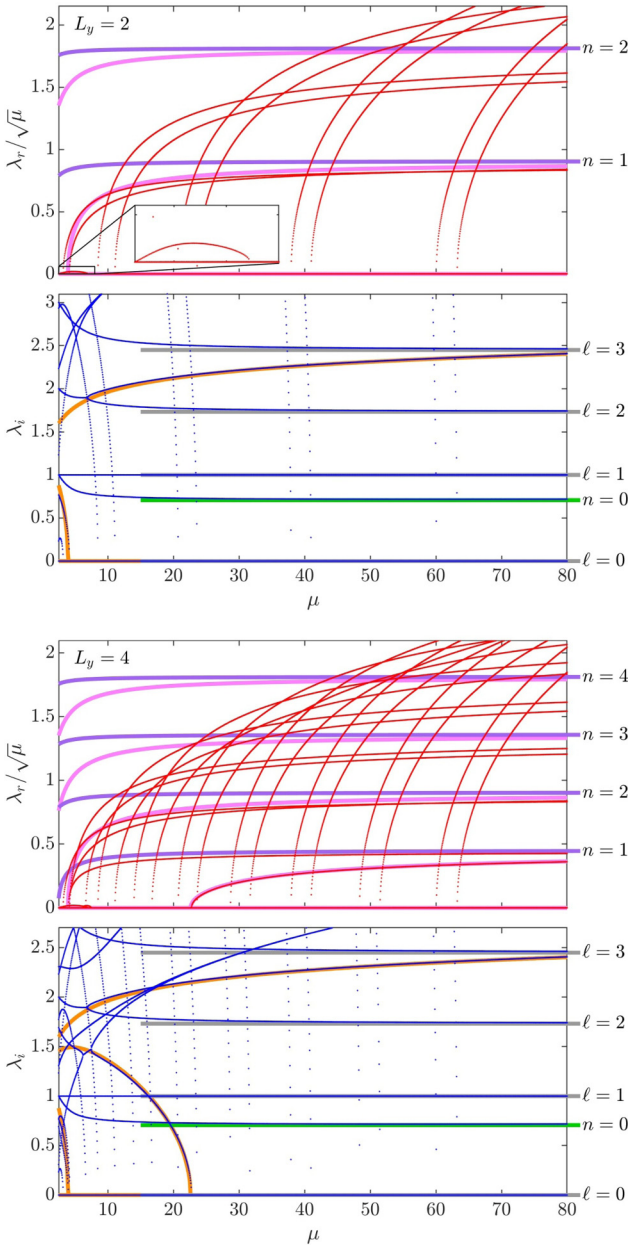


FIG. 3. Comparison between the two dark soliton stripes' stability spectra for the full GPE and the analytical prediction based on the AI PDE. Depicted are the real (λ_r; top subpanels) and imaginary (λ_i; bottom subpanels) parts of the stability eigenvalues, $\lambda = \lambda_r + i\,\lambda_i$, vs the chemical potential μ (note that λ_r is scaled by $\sqrt{\mu}$). For the numerical domain we use $L_x = 16$ as well as $L_y = 2$ (top set of panels) and $L_y = 4$ (bottom set of panels). In the top subpanels (displaying λ_r) the real part of the eigenvalues from the full GPE is depicted by the small red dots, while the thick pink (light gray) curves depict the real part of the eigenvalues for the effective AI PDE model and the thick violet (dark gray) curves depict the (unstable) $n \geqslant 1$ in-phase modes; see Eq. (9). In the bottom subpanels (displaying λ_i) the imaginary part of the eigenvalues from the full GPE is depicted by the small blue dots, while the thick orange (light gray) curves depict the real part of the eigenvalues for the effective AI PDE model, the thick green (dark gray) horizontal line depicts the single-stripe $n = 0$ (stable) in-phase mode $\mathrm{Im}(\lambda) = \Omega/\sqrt{2}$, and the thick gray horizontal lines correspond to the 1D TF spectrum; see Eq. (8).

enough L_y, no unstable wavelengths will fit in the domain and the solutions will be effectively stable in a manner akin to the stabilization of transverse dark solitons in elongated BECs reported in Ref. [28]. Therefore, we have selected two typical L_y values to compare the BdG-GPE and AI PDE. The results for $L_y = 2$ and $L_y = 4$ are shown in Fig. 3 (see top and bottom sets of panels, respectively). As can be seen from the figure, all of the AI PDE modes referring to the soliton stripes are also present in the original BdG-GPE.

It is crucial to note that the AI PDE cannot capture modes referring to the background (stripeless configuration). These background modes correspond to both longitudinal and transverse modes. The longitudinal background modes in our system correspond to the collective oscillations of a 1D trapped BEC, characterized by the imaginary eigenvalues $\lambda_\ell = i\omega_\ell$, where the corresponding frequencies are given by [51]

$$\omega_\ell = \sqrt{\frac{\ell(\ell+1)}{2}}\,\Omega. \tag{8}$$

Note that, in our notation, instabilities are characterized by a positive real part of the eigenvalue λ, which in turn corresponds to an imaginary part of the corresponding eigenfrequency ω. The frequencies of the longitudinal background modes are depicted by the thick gray horizontal lines in Fig. 3, which give a good approximation of the corresponding frequencies of the full BdG-GPE modes, especially as μ becomes larger. Another set of modes that the AI PDE is not able to capture corresponds to in-phase (IP) oscillating dark soliton stripes (hereafter, these will be called IP modes). Nevertheless, one can approximate the relevant oscillation frequency as follows. According to the AI analysis the oscillatory modes of a *single* dark soliton in a 1D trap are characterized by the frequencies [36] (see also Ref. [49])

$$\lambda_n = i\,\omega_n = \sqrt{\frac{1}{3}\mu k_n^2 - \frac{1}{2}\Omega^2}, \tag{9}$$

where $k_n = n\pi/L_y$. Then, for in-phase oscillating soliton stripes and large chemical potentials, one may approximate the oscillation frequency of the relevant IP modes by Eq. (9). This is because for such IP modes the distance between the stripes remains the same during the evolution, and thus the interaction (depending on their relative distance) effectively does not affect the motion. These modes are depicted by the violet curves in Fig. 3. A relevant example concerns the appearance of the important stable IP mode, namely the $k_n = 0$ mode (see thick green line) in the full BdG-GPE spectrum shown in Fig. 3. The eigenfrequency of this mode corresponds to the oscillation frequency $\mathrm{Im}(\lambda) = \Omega/\sqrt{2}$ of a single [52] or multiple in-phase [18] solitons. However, one should not expect that the frequencies of the IP modes in the full BdG-GPE will be identical to ω_n in Eq. (9). This results in the *collective* oscillation for the multisoliton stripe state to have a frequency that is slightly larger than the single-dark-soliton prediction (9). Here it should be pointed out that the convergence of the full BdG-GPE and the $n = 0$ IP modes in the TF limit, as shown in Fig. 3, can simply be understood as follows: as μ increases, the interactions become increasingly short-ranged and, hence, the solitons are

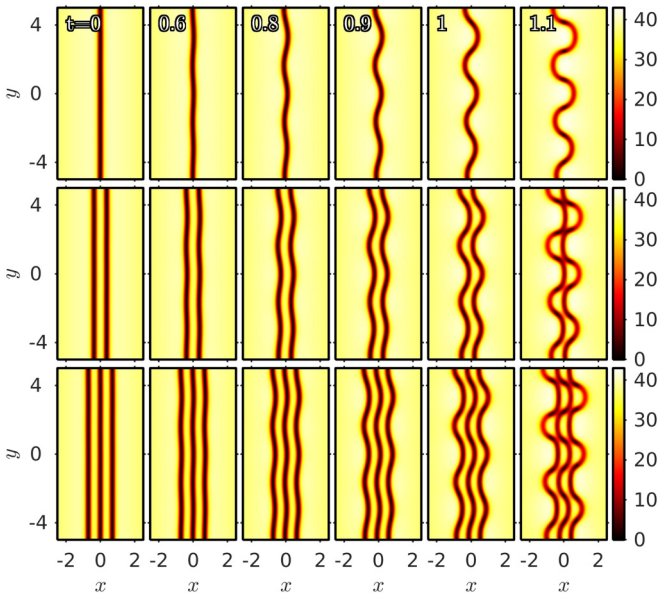


FIG. 4. Dynamics for in-phase modes corresponding, from top to bottom, to the one-, two-, and three-stripe states for $\mu = 40$. The color bars on the right-hand side correspond to the density $|u(x, y, t)|^2$. The system was initialized at $t = 0$ with an N-stripe state perturbed by the mode $A\cos(k_n y)$ in the transverse direction, where $k_n = n\pi/L_y$ with $A = 10^{-3}$, $n = 5$, and $L_y = 8$ (only the portion corresponding to $-5 \leqslant y \leqslant 5$ at the times indicated is shown). Note that the dynamics, including the growth rate, seem to be closely analogous in the different cases.

all pushed towards the center of the trap. Thus, they should all oscillate with the same IP frequency ($\Omega/\sqrt{2}$) at the bottom of the well. We shall see this mode again when we generalize to three and four stripes in the next subsection.

The lower the order n of the mode, the better the approximation in Eq. (9) is, and all results asymptotically match as $\mu \to \infty$. It is evident that the modes of the full BdG-GPE analysis arise in pairs, i.e., IP and OOP for the case of two stripes. Similarly, we will see below that the modes arise in triplets for three stripes, groups of 4 for four stripes, etc. Among these, we have confirmed that the lowest growth rate corresponds to the IP excitation, while the higher growth rate corresponds to the OOP one.

An example of the relevant dynamics of in-phase evolution of multisoliton stripes is depicted in Fig. 4 for the case of the $n = 5$ IP mode for one, two, and three stripes and for a relatively large chemical potential $\mu = 40$. As can be seen from the figure, the instability evolutionary dynamics (and thus the associated growth rates) seem to be largely independent of the number of stripes. Furthermore, the actual destabilization evolution of the stripes even in the nonlinear regime (but before the stripes break into pairs of vortices) seems to also be largely independent of the number of stripes. Hence, the IP mode excitations behave similarly to the case of a single stripe.

Finally, concerning the spectra, it is worth mentioning that there exist other eigenmodes corresponding to the background (rather than the dark soliton stripes). For instance, there exist imaginary eigenvalues that appear in pairs (starting at the linear limit) and that monotonically increase as a function of μ. These eigenvalue pairs seem to quickly approach (asymptotically) each other as μ is increased (for the $L_y = 4$ case they visually coalesce around $\mu \approx 20$; see the relevant monotonically increasing blue curves in the bottom panel of Fig. 3). Each of these eigenmode pairs corresponds to undulations of the background's edges, where the left and right ends oscillate with progressively higher wave numbers as the mode frequency increases. These oscillations are in or out of phase between the two edges (at opposite x's), yet as the chemical potential increases, and so does the separation between the edges, the former and latter tend to oscillate with the same frequency. We do not describe further these modes as they only pertain to benign (i.e., purely oscillatory) perturbations away from the dark soliton stripes.

With the above observations in mind, let us now summarize a number of key features of the multistripe spectra:

(1) Our theory correctly captures with good accuracy the *stable* $n = 0$ out-of-phase (OOP) oscillation mode (see analysis in the end of Sec. II) of the two stripes, in line with the pertinent 1D theory [49].

(2) The oscillation frequency of the stable $n = 0$ in-phase (IP) mode for the two-stripe state can be well approximated by the frequency for the one-stripe state in the trap; this is confirmed in the full BdG-GPE spectrum.

(3) Our theory detailed above in Sec. II only captures the OOP modes. The IP modes appear to be independent of the interaction, and hence essentially equivalent to the single-stripe results of Ref. [36] in the TF limit. This also refers to the three- and four-stripe cases (see below).

(4) Each of the finite k_n transverse wave number modes, compared with the single-stripe case, splits into two. This has a natural explanation as the number of stripe degrees of

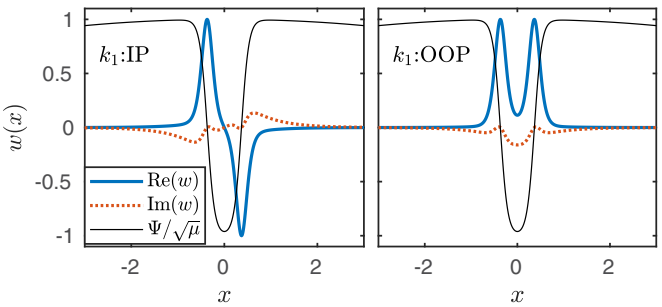


FIG. 5. Eigenfunctions corresponding to the in-phase (IP; left) and out-of-phase (OP; right) unstable modes of the stationary two-stripe state $\Psi(x)$ for $L_y = 2$ and $\mu = 40$. Shown are the k_1 modes with transverse dependence given by $\cos(k_n y)$ with $k_n = n\pi/L_y$. The eigenmodes corresponding to other values of n are very similar (results not shown here). The thick solid (blue) and dotted (red) lines correspond, respectively, to the real and imaginary parts of the eigenfunction $w(x)$. The corresponding normalized steady state, $\Psi(x)/\sqrt{\mu}$, is depicted by the thin black line. Note that the real part of the eigenmodes has localized "humps" that, when out of phase, produce in-phase motion of the dark solitons and vice versa. The reason for this apparent contradiction is that the dark solitons are themselves of opposite phase: in this figure the left soliton corresponds to $-\tanh$ while the right one corresponds to $+\tanh$.

freedom has been doubled. In a similar vein, there are three sets of branches for the three-stripe case and four branches for the four-stripe case (see below). In Fig. 5 we depict the longitudinal dependence of the IP and OOP modes extracted from the full BdG-GPE. As expected, for two stripes there are two "normal" modes for each k_n corresponding to the IP and OOP ones.

(5) Despite the increase in the multiplicity of the normal modes, different normal modes of the same k_n mode have similar growth rates, which are also similar to those of a single dark soliton stripe. Therefore, the increase of the number of solitons creates more instabilities, but does not substantially increase the instability growth rate. Nevertheless, as we will show below, for large μ there is a monotonic (albeit weak) increase of the growth rate of the instabilities with the stripe number. It also appears that the branches of the same unstable k_n mode for the two stripes converge together in the TF limit.

(6) There is also one interesting difference near the linear limit. In contrast to the single stripe, which has a narrow fully stable regime near the linear limit, many stripes (including the following cases of three and four stripes) studied here all become unstable right from the linear limit. Note the small "bumps" in λ_r near the linear limits (see inset in the top panel in Fig. 3). This instability is analogous to the one observed in the corresponding quasi-1D [18] and 1D [49] cases, arising from opposite energy mode collision and associated with complex eigenvalues. However, before the latter is stabilized (as in 1D), transverse modes start yielding unstable growth (via real eigenvalues). This causes the multistripe configurations to be susceptible to

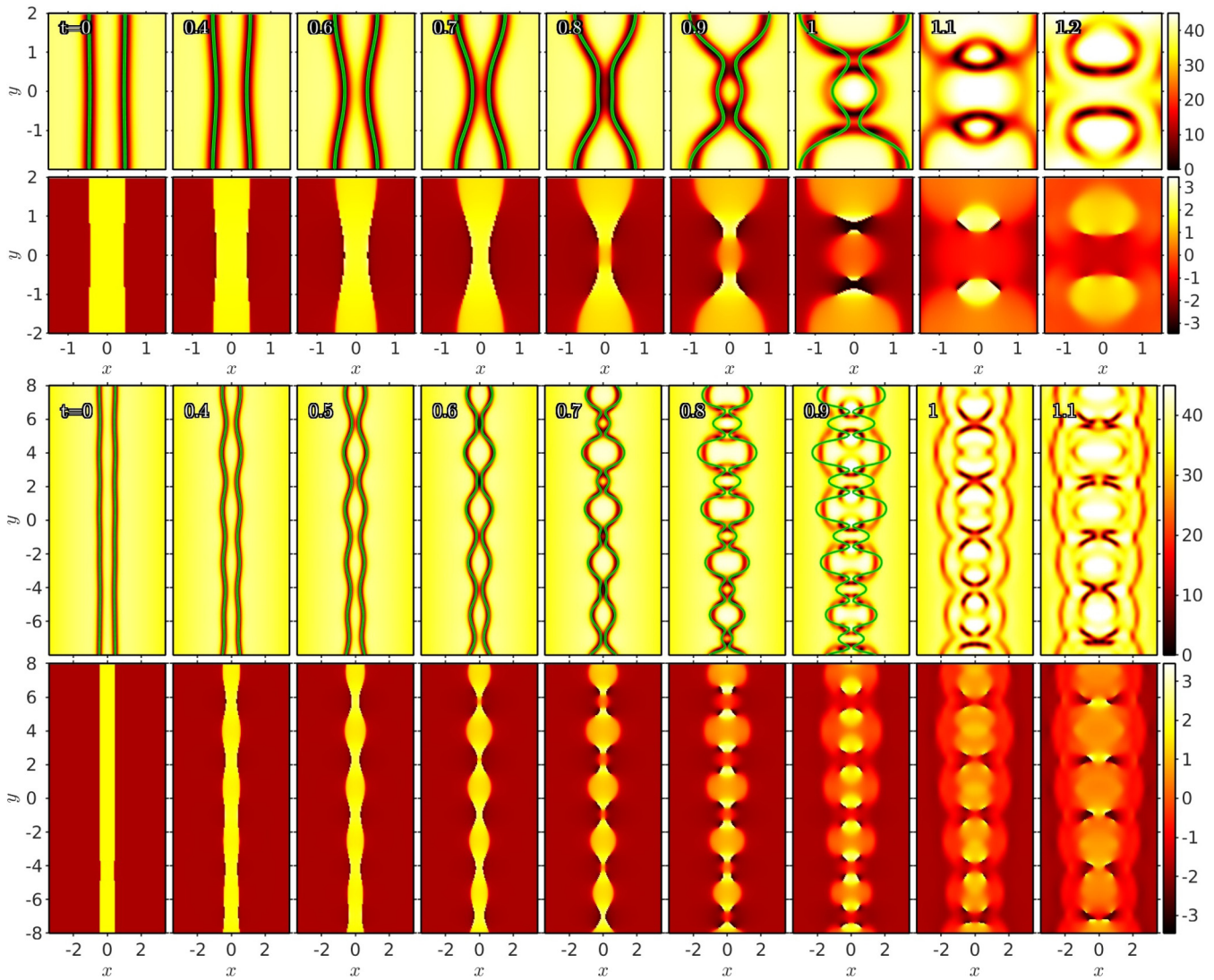


FIG. 6. Dynamical destabilization and collision of two dark soliton stripes. The background color map corresponds to full GPE numerics while the green overlaid curves correspond to the AI reduction The corresponding systems are initialized symmetrically with the right dark soliton stripe at $x_0(y) = \xi_0 + \sum_{n=1}^{\nu} \varepsilon_n \sin(2\pi n y/L_y + \varphi_n)$ with $\varepsilon_n = 0.01$, $\varphi_n = (n-1)L_y\pi/10$, $\xi_0 = 0.45$ (i.e., close to the steady state equilibrium $x_0^{(\mathrm{eq})} = 0.368$), and $\mu = 40$. The top two rows of panels correspond to a single-mode perturbation ($\nu = 1$) with $L_y = 2$ while the bottom two rows of panels correspond to a perturbation containing five modes ($\nu = 5$) and $L_y = 8$. Within each set of panels the top and bottom rows (and their color bars) correspond to the density $[|u(x, y, t)|^2]$ and phase ($-\pi$ to π) of the field at the indicated times.

instability for *all* the values of chemical potentials considered herein.

The results presented above indicate that the AI PDE is able to approximate very well the (linear OOP) modes that it is designed to capture. However, our ultimate goal with the AI method is not only to obtain the BdG modes, but more importantly to obtain a reduced AI PDE that is also able to capture the (linear and) nonlinear dynamics of the stripe dynamics. We therefore now compare the dynamics of the full GPE and of the AI PDE. We initialize typical symmetric stripes of the form

$$x_0(y, t = 0) = \pm[\xi_0 + p(y)], \tag{10}$$

where ξ_0 is the initial location of the stripes and $p(y)$ is a perturbation to accelerate the destabilization dynamics. We depict in Fig. 6 two typical cases that compare the full GPE dynamics (see background color map) and the AI PDE dynamics (see overlaid green curves). The first case (see top set of panels) corresponds to an initial position close to stationary equilibrium $x_0^{(\mathrm{eq})}$ perturbed by a single mode ($n = 1$ for $L_y = 2$) with amplitude 0.01. The second case (see bottom set of panels) corresponds to the same initial position of the stripe but now perturbed by five different modes (see caption for more details); see figure caption for details on the perturbation $p(y)$ used in these two cases. As can be noticed from the figure, for both cases, the AI PDE is able to capture (a) the initial growth of the perturbation (in accordance with our previous results on the BdG spectra), (b) the strong interactions between the stripes that include collision and bounce-back, and importantly (c) even some of the nonlinear stripe dynamics before the stripes finally break into vortices. It is remarkable that indeed the AI PDE is able to capture the full GPE dynamics even when the stripes are interacting quite strongly.

C. Three- and four-stripe states

In this section, we consider the cases of three- and four-stripe states, and study their spectra and dynamics. The dependence of the real and imaginary parts of the eigenvalues on the chemical potential is shown in Fig. 7 for both cases. Besides the presence of the same background modes as the ones described above for the two-stripe case, we can clearly see the multiplicity of the interstripe vibrational modes. The three-stripe case has three modes while the four-stripe case has four. As explained above, this multiplicity stems from the different normal modes of vibration of the N-stripe solution. Indeed, we have extracted the longitudinal dependence of the normal modes for $n = 2$ as depicted in Fig. 8. As can be observed from the figure, the three- and four-stripe cases have, respectively, three and four normal modes.

It is also evident, more so in the three- and four-stripe cases when compared to the two-stripe case, that in comparison, e.g., with Fig. 2 of Ref. [36], the higher N is, the more unstable the corresponding state becomes in the TF limit. This makes intuitive sense, as the differential repulsion of the stripes at different locations (in the presence of perturbations) can be expected to lead to enhancement of the undulations and ultimately of the instability growth rate. This is more concretely quantified in Fig. 9. The top panel clearly shows

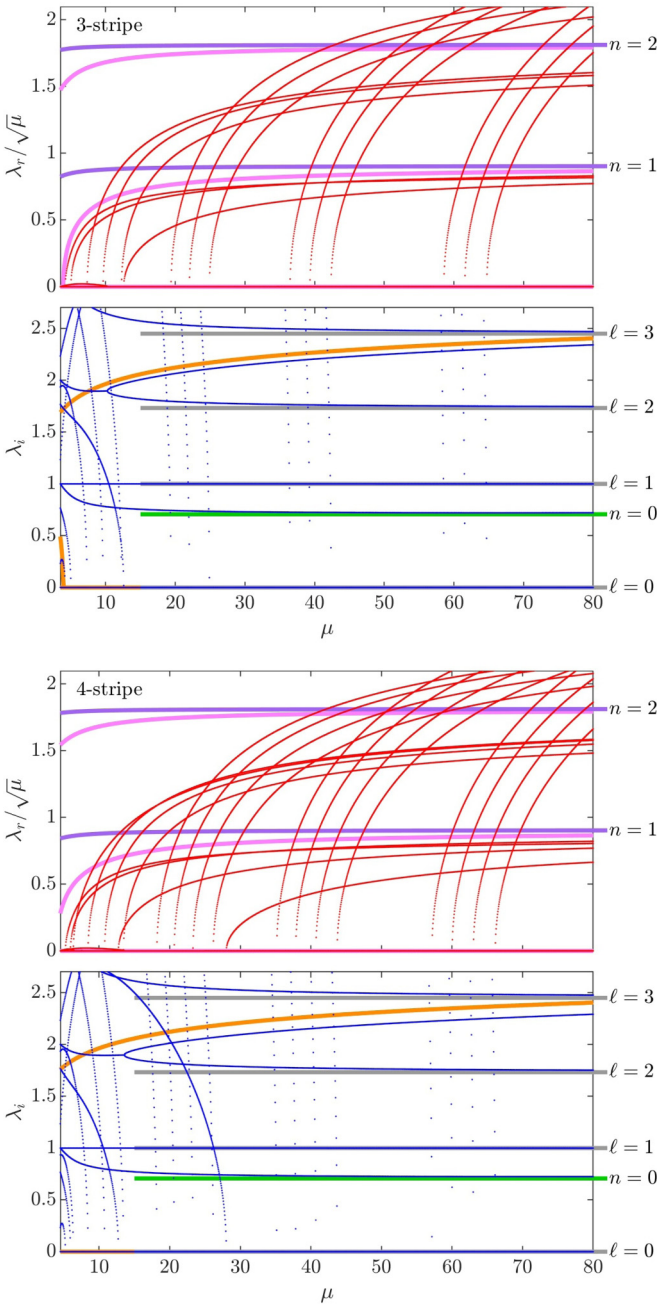


FIG. 7. Similar to Fig. 3 (for two stripes), but now for the three- and four-stripe cases, for $L_x = 16$ and $L_y = 2$.

that the IP modes converge, in the TF limit, to the same frequency of IP oscillations for the different stripes. On the other hand, the bottom panel shows, interestingly, that the single-stripe state is the one that bifurcates into instability the earliest. Nevertheless, and going towards the analytically tractable limit of large μ, we observe that there exists a crossover. As a result, more soliton stripes lead to higher—but only slightly higher—growth rates. Nevertheless, the scales of the growth rates of different numbers of stripes remain quite proximal.

Finally, we have performed simulations to study the dynamics when random noise is added to the stationary state. In this case we do not compare with the AI PDE dynamics

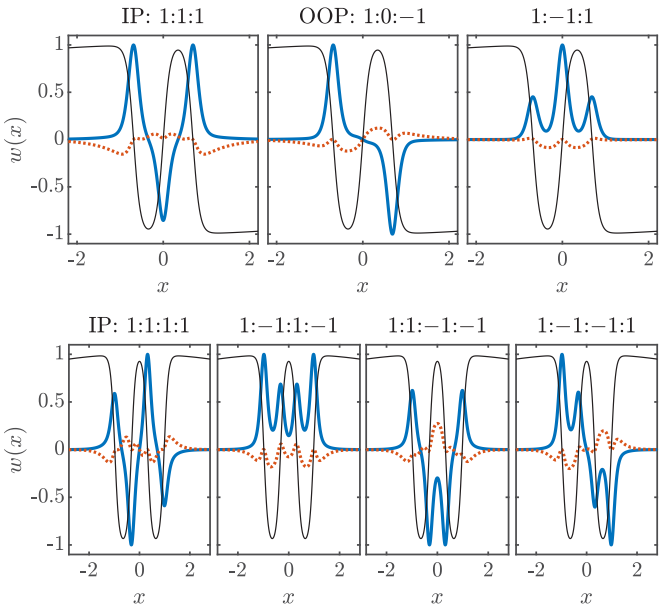


FIG. 8. Same as Fig. 5 but for the three-stripe (top) and four-stripe (bottom) states. Parameters correspond to $L_y = 2$ and $\mu = 40$ for the transverse modes involving the motion of the dark soliton stripes. The notation $\pm 1 : \pm 1 : \pm 1$ is used to denote a normal mode that has a displacement from the steady state of the first, second, and third dark solitons in the positive (+) or negative (−) direction. The same notation is used for the four-stripe case.

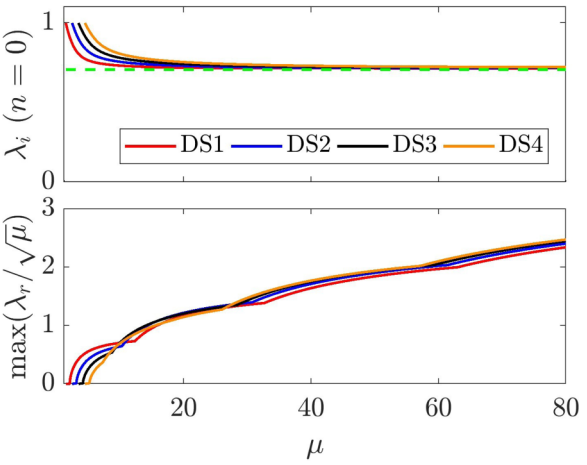


FIG. 9. Top panel: Comparison of the fully in-phase oscillation mode ($n = 0$) frequency for different numbers of dark soliton stripes using the same $L_y = 2$. DSN denotes the N-stripe state. Note that they all converge to the 1D single dark soliton results $\Omega/\sqrt{2}$ (see horizontal dashed line) corresponding to the IP oscillation of the N stripes. Bottom panel: The most unstable mode growth rate for different numbers of dark soliton stripes. Note there is an interesting crossover behavior. The growth rate is larger for the one-stripe state near the linear limit, but in the TF limit more dark solitons are more unstable. Moreover, in the latter limit there is a (weak, yet) monotonic increase of the growth rate with N. The DS1, DS2, DS3, and DS4 cases are depicted, respectively, with the red (gray), blue (dark gray), black, and yellow (light gray) curves.

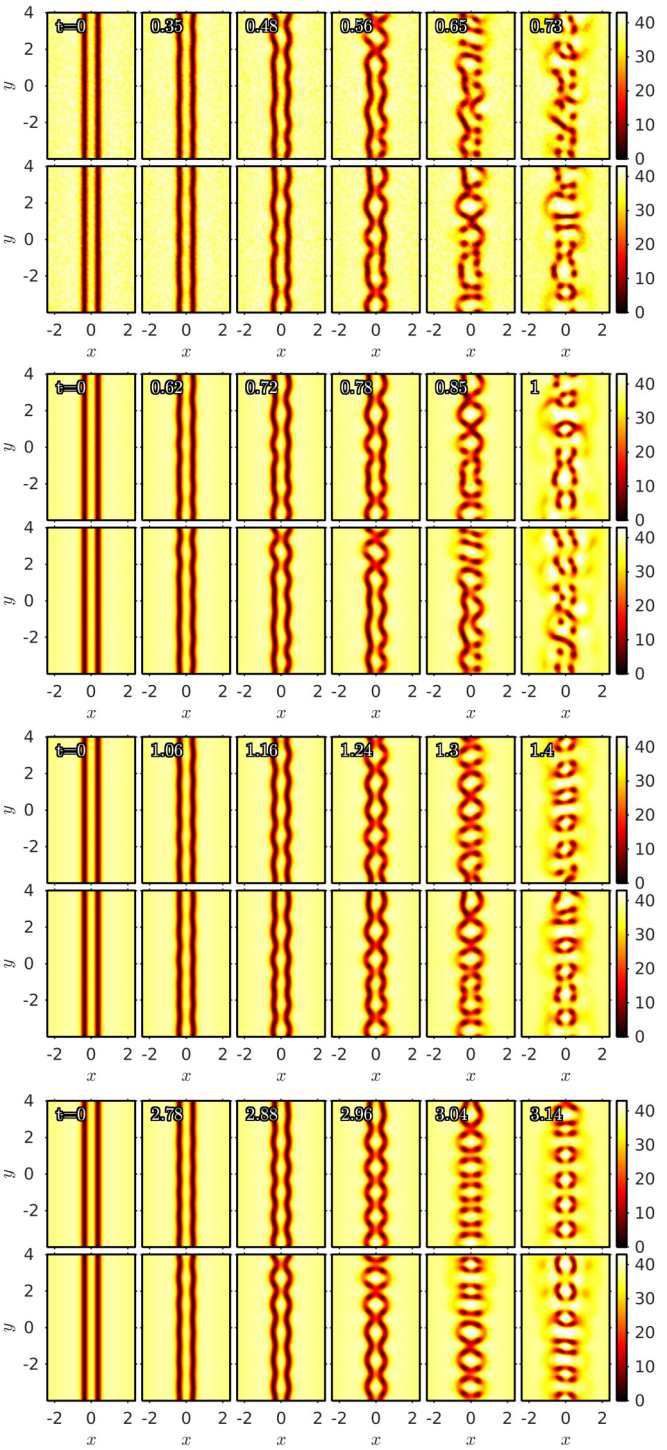


FIG. 10. Dynamical destabilization of two-stripe states using different small random perturbations. Each set of two rows of panels corresponds, from top to bottom, to two different realizations for a random perturbation of amplitude 10^{-1}, 10^{-2}, 10^{-4}, and 10^{-12}, respectively.

as our analytical characterization captures the OOP modes (in terms of their nonlinear dynamics) but not the IP ones. Given that random perturbations excite both, a more elaborate and less straightforwardly tractable AI approach without the assumption of symmetric center positions would be needed for comparison here. In Fig. 10 we depict the dynamics

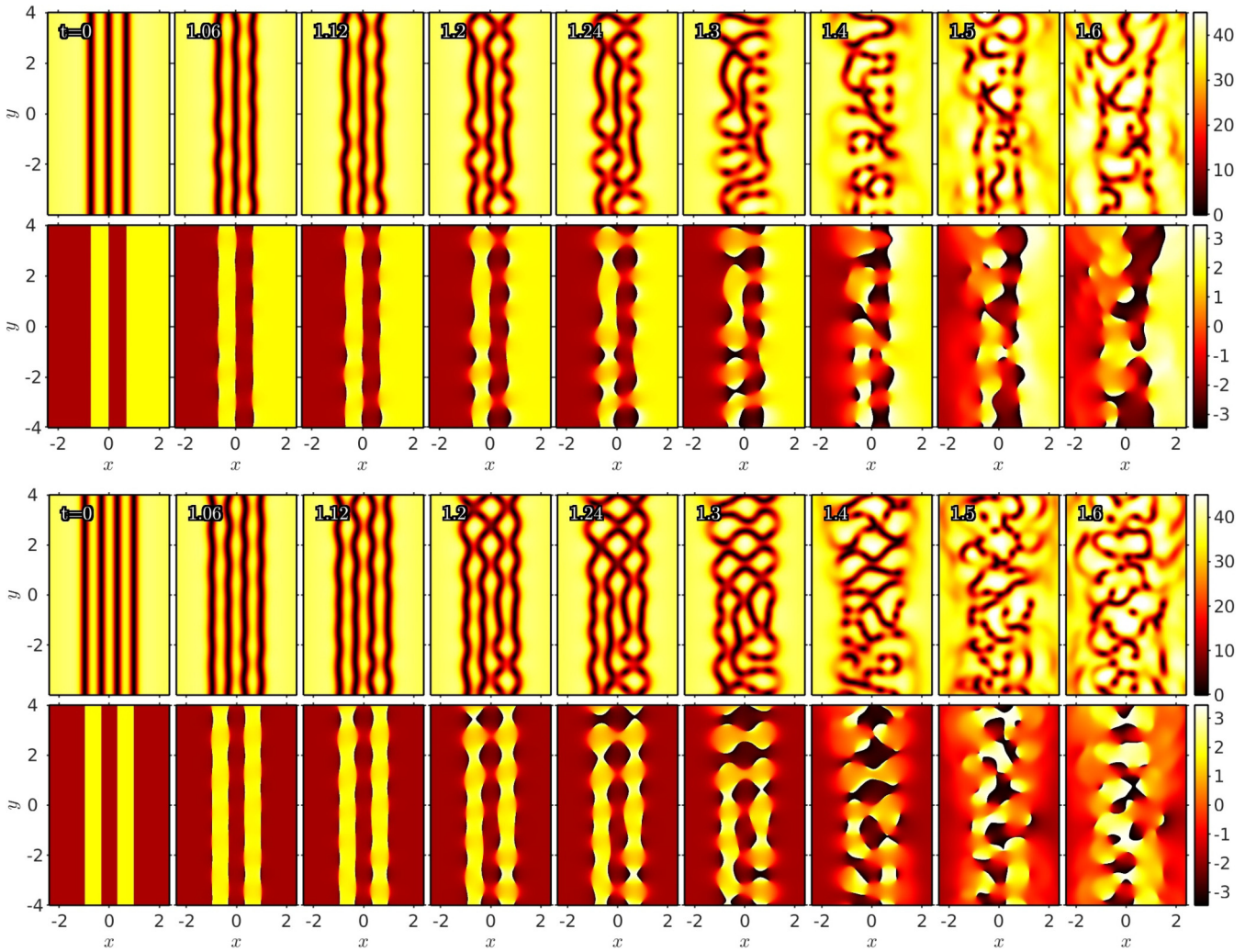


FIG. 11. Dynamical destabilization of the three- and four-stripe states as obtained from the full GPE. In these cases, we have added a small (10^{-4} amplitude) random noise. Both states, following the spectral picture, break with the most unstable mode, and give rise to numerous vortex pairs. Note that, despite the existence of more unstable modes, the maximum decay rates are about the same for different numbers of stripes.

ensuing from the two-stripe state perturbed by a small, uniformly distributed random perturbation. For each perturbation size we show two typical runs and, from top to bottom, we depict the cases for random perturbations of diminishing amplitude. Surprisingly, as the perturbation is set to smaller values, the full GPE dynamics tends to a *symmetric OOP* configuration for the two stripes.

In Fig. 11 we depict the dynamical destabilization for the three- and four-stripe cases. The BdG spectra depicted in Fig. 7, computed for $L_y = 2$, suggest that the dominant unstable mode for $\mu = 40$ should be the $n = 3$ one which corresponds to the $n = 6$ mode in Fig. 11, as in this latter case we used $L_y = 4$. The dynamics indeed follows this prediction until each stripe breaks into vortex pairs. It is, arguably, not entirely straightforward to define a precise breaking time, as this is a continuous process, but both states start to bend around $t = 1$ and therefore the two states break at about the same timescale, as expected from the spectra. It should be noted that, for the three-stripe case, the AI approach is conceptually straightforward to construct, generalizing the energy functional of Eq. (5), because for OOP configurations the dark soliton in the middle is centered at $x = 0$ and the relevant center positions are $-x_0$, 0, and x_0. However, the resulting expressions are particularly tedious and hence we do not attempt to give them here.

We now comment on the possibility of generating quantum turbulence from the transverse-instability-induced dynamics of multiple dark soliton stripe states. This scenario was considered and investigated in Ref. [30] for an initial configuration different from that used in this work, namely for a square grid of many dark soliton stripes in a spatially uniform condensate. In our case, Fig. 11 (see panels corresponding to $t = 1.6$) suggests that the instability-induced generation of vorticity could also lead to quantum turbulence. Nevertheless, the state of quantum turbulence that is induced by the decay of a series of dark soliton stripes is likely to lack the vortex clustering, as well as the statistical signatures of classical and quantum two-dimensional turbulence [53–55]. Nonetheless, weak correlations and small clusters can build after some vortex-antivortex annihilation [56], which we surmise is one

of the more interesting effects that could be observed for this type of turbulent state. In any case, a pertinent systematic study of such effects is beyond the scope of this work.

IV. CONCLUSIONS AND FUTURE WORK

In the present work, we have extended considerations of the solitonic stripes as filaments to the realm of multiple stripes, taking into consideration their pairwise interactions. We have seen how this allows one to evaluate the equilibrium position of multistripe states. Perhaps more importantly, this also enables the consideration of the linearized eigenmodes around such an equilibrium. These modes can be partitioned into in-phase and out-of-phase ones. The in-phase ones are similar to the single-stripe modes. On the other hand, the out-of-phase ones introduce additional growth modes of the transverse instability. Despite the larger number of instabilities, the maximum growth rates remain comparable to that of a single stripe, although we have found a weak monotonic dependence thereof on the number of stripes N in the large chemical potential limit. In addition to this linearization picture, we have explored the full dynamics of the two stripes, which are always in the cases examined in good agreement with the filament (AI PDE) method results that consider each of the stripes as a reduced PDE for the stripe center $x_0(y,t)$. We have extended the numerical consideration of such stripe interaction scenarios to the case of three- and four-stripe settings, obtaining a natural generalization of the two-stripe results.

This effort paves the way for a number of future possibilities. One of the most intriguing ones, in line with the experimental thesis results of Ref. [29], is to examine the interaction of a quasi-1D pattern (like the stripe) and a genuinely 2D pattern, like the vortex. This has been associated with a nonlinear variant of the famous Aharonov-Bohm effect in Refs. [57,58]. Yet, it has not been systematically explored at the level of a filament theory such as the one presented herein, which could shed quantitative light in the relevant dynamics. Moreover, this is an especially appealing problem at the interface of dimensionalities and at the interface between differential and integral equations (preliminary calculations suggest that the vortex has a distributed effect on the stripe, while the stripe has an integrated effect on the motion of the vortex). A version of this problem that could be radially symmetric and hence simpler to tackle could be that of a ring dark soliton with a vortex sitting in its center. One can also go beyond 2D settings and consider effective PDEs for 1D filaments such as vortex rings embedded in 3D space, as in the recent works of Refs. [59,60], and then attempt to generalize these incorporating ring-ring interaction to account for multi-vortex-ring settings [61–63]. These directions will be considered in future studies.

ACKNOWLEDGMENTS

W.W. acknowledges support from the Swedish Research Council under Grant No. 642-2013-7837 and from the Goran Gustafsson Foundation for Research in Natural Sciences and Medicine. P.G.K. gratefully acknowledges the support of NSF-PHY-1602994, as well as from the Greek Diaspora Fellowship Program. R.C.-G. gratefully acknowledges the support of NSF-PHY-1603058. B.P.A. gratefully acknowledges the support of NSF-PHY-1607243.

[1] Yu. S. Kivshar and B. Luther-Davies, Phys. Rep. **298**, 81 (1998).
[2] D. J. Frantzeskakis, J. Phys. A: Math. Theor. **43**, 213001 (2010).
[3] P. G. Kevrekidis, D. J. Frantzeskakis, and R. Carretero-González, *The Defocusing Nonlinear Schrödinger Equation: From Dark Solitons and Vortices to Vortex Rings* (SIAM, Philadelphia, 2015).
[4] B. Denardo, B. Galvin, A. Greenfield, A. Larraza, S. Putterman, and W. Wright, Phys. Rev. Lett. **68**, 1730 (1992).
[5] P. Marquie, J. M. Bilbault, and M. Remoissenet, Phys. Rev. E **49**, 828 (1994).
[6] M. Chen, M. A. Tsankov, J. M. Nash, and C. E. Patton, Phys. Rev. Lett. **70**, 1707 (1993); B. A. Kalinikos, M. M. Scott, and C. E. Patton, *ibid.* **84**, 4697 (2000).
[7] A. B. Kozyrev and D. W. van der Weide, J. Phys. D: Appl. Phys. **41**, 173001 (2008); Z. Wang, Y. Feng, B. Zhu, J. Zhao, and T. Jiang, J. Appl. Phys. **107**, 094907 (2010); L. Q. English, S. G. Wheeler, Y. Shen, G. P. Veldes, N. Whitaker, P. G. Kevrekidis, and D. J. Frantzeskakis, Phys. Lett. A **375**, 1242 (2011).
[8] V. Achilleos, O. Richoux, G. Theocharis, and D. J. Frantzeskakis, Phys. Rev. E **91**, 023204 (2015); J. Zhang, V. Romero-García, G. Theocharis, O. Richoux, V. Achilleos, and D. J. Frantzeskakis, Appl. Sci. **8**, 1186 (2018).
[9] A. Chabchoub, O. Kimmoun, H. Branger, N. Hoffmann, D. Proment, M. Onorato, and N. Akhmediev, Phys. Rev. Lett. **110**, 124101 (2013); A. Chabchoub, O. Kimmoun, H. Branger, C. Kharif, N. Hoffmann, M. Onorato, and N. Akhmediev, Phys. Rev. E **89**, 011002(R) (2014).
[10] P. K. Shukla and B. Eliasson, Phys. Rev. Lett. **96**, 245001 (2006); R. Heidemann, S. Zhdanov, R. Sütterlin, H. M. Thomas, and G. E. Morfill, *ibid.* **102**, 135002 (2009).
[11] A. Piccardi, A. Alberucci, N. Tabiryan, and G. Assanto, Opt. Lett. **36**, 1356 (2011).
[12] Y. V. Kartashov and L. Torner, Opt. Lett. **32**, 946 (2007); Q. Kong, Q. Wang, O. Bang, and W. Krolikowski, Phys. Rev. A **82**, 013826 (2010); G. Assanto, T. R. Marchant, A. A. Minzoni, and N. F. Smyth, Phys. Rev. E **84**, 066602 (2011); T. P. Horikis and D. J. Frantzeskakis, Phys. Rev. Lett. **118**, 243903 (2017).
[13] T. Bland, M. J. Edmonds, N. P. Proukakis, A. M. Martin, D. H. J. O'Dell, and N. G. Parker, Phys. Rev. A **92**, 063601 (2015); T. Bland, K. Pawlowski, M. J. Edmonds, K. Rzazewski, and N. G. Parker, *ibid.* **95**, 063622 (2017).
[14] K. G. Lagoudakis, T. Ostatnický, A. V. Kavokin, Y. G. Rubo, R. André, and B. Deveaud-Plédran, Science **326**, 974 (2009); G. Grosso, G. Nardin, F. Morier-Genoud, Y. Léger, and B. Deveaud-Plédran, Phys. Rev. Lett. **107**, 245301 (2011);

V. Goblot, H. S. Nguyen, I. Carusotto, E. Galopin, A. Lemaitre, I. Sagnes, A. Amo, and J. Bloch, *ibid.* **117**, 217401 (2016); X. Ma, O. A. Egorov, and S. Schumacher, *ibid.* **118**, 157401 (2017).

[15] P. Engels and C. Atherton, Phys. Rev. Lett. **99**, 160405 (2007).

[16] C. Becker, S. Stellmer, P. Soltan-Panahi, S. Dörscher, M. Baumert, E.-M. Richter, J. Kronjäger, K. Bongs, and K. Sengstock, Nat. Phys. **4**, 496 (2008).

[17] A. Weller, J. P. Ronzheimer, C. Gross, J. Esteve, M. K. Oberthaler, D. J. Frantzeskakis, G. Theocharis, and P. G. Kevrekidis, Phys. Rev. Lett. **101**, 130401 (2008).

[18] G. Theocharis, A. Weller, J. P. Ronzheimer, C. Gross, M. K. Oberthaler, P. G. Kevrekidis, and D. J. Frantzeskakis, Phys. Rev. A **81**, 063604 (2010).

[19] B. P. Anderson, P. C. Haljan, C. A. Regal, D. L. Feder, L. A. Collins, C. W. Clark, and E. A. Cornell, Phys. Rev. Lett. **86**, 2926 (2001).

[20] I. Shomroni, E. Lahoud, S. Levy, and J. Steinhauer, Nat. Phys. **5**, 193 (2009).

[21] C. Becker, K. Sengstock, P. Schmelcher, R. Carretero-González, and P. G. Kevrekidis, New J. Phys. **15**, 113028 (2013).

[22] S. Serafini, M. Barbiero, M. Debortoli, S. Donadello, F. Larcher, F. Dalfovo, G. Lamporesi, and G. Ferrari, Phys. Rev. Lett. **115**, 170402 (2015).

[23] P. G. Kevrekidis and D. J. Frantzeskakis, Rev. Phys. **1**, 140 (2016).

[24] A. Negretti and C. Henkel, J. Phys. B: At. Mol. Opt. Phys. **37**, L385 (2004); A. Negretti, C. Henkel, and K. Mølmer, Phys. Rev. A **78**, 023630 (2008).

[25] M. I. Shaukat, E. V. Castro, and H. Terças, Phys. Rev. A **95**, 053618 (2017).

[26] E. A. Kuznetsov and S. K. Turitsyn, Zh. Eksp. Teor. Fiz. **94**, 119 (1988) [Sov. Phys. JETP **67**, 1583 (1988)].

[27] Yu. S. Kivshar and D. E. Pelinovsky, Phys. Rep. **331**, 117 (2000).

[28] I. Morera Navarro, M. Guilleumas, R. Mayol, and A. Muñoz Mateo, Phys. Rev. A **98**, 043612 (2018).

[29] K. Wilson, Developing a toolkit for experimental studies of two-dimensional quantum turbulence in Bose–Einstein condensates, Ph.D. thesis, University of Arizona, 2015 (unpublished).

[30] T. Kusumura, M. Tsubota, and H. Takeuchi, J. Phys.: Conf. Ser. **400**, 012038 (2012).

[31] V. Tikhonenko, J. Christou, B. Luther-Davies, and Yu. S. Kivshar, Opt. Lett. **21**, 1129 (1996).

[32] V. A. Mironov, A. I. Smirnov, and L.A. Smirnov, Zh. Eksp. Teor. Fiz. **139**, 55 (2011) [Sov. Phys. JETP **112**, 46 (2011)].

[33] M. A. Hoefer and B. Ilan, Phys. Rev. A **94**, 013609 (2016).

[34] M. Ma, R. Carretero-González, P. G. Kevrekidis, D. J. Frantzeskakis, and B. A. Malomed, Phys. Rev. A **82**, 023621 (2010); see also references therein.

[35] P. G. Kevrekidis, Wenlong Wang, R. Carretero-González, and D. J. Frantzeskakis, Phys. Rev. Lett. **118**, 244101 (2017).

[36] P. G. Kevrekidis, Wenlong Wang, R. Carretero-González, and D. J. Frantzeskakis, Phys. Rev. A **97**, 063604 (2018).

[37] Yu. S. Kivshar and X. Yang, Phys. Rev. E **50**, R40(R) (1994).

[38] D. Neshev, A. Dreischuh, V. Kamenov, I. Stefanov, S. Dinev, W. Fliesser, and L. Windholz, Appl. Phys. B **64**, 429 (1997); A. Dreischuh, D. Neshev, G. G. Paulus, F. Grasbon, and H. Walther, Phys. Rev. E **66**, 066611 (2002).

[39] T. P. Horikis and D. J. Frantzeskakis, Opt. Lett. **41**, 583 (2016).

[40] G. Theocharis, D. J. Frantzeskakis, P. G. Kevrekidis, B. A. Malomed, and Yu. S. Kivshar, Phys. Rev. Lett. **90**, 120403 (2003).

[41] G. Theocharis, P. Schmelcher, M. K. Oberthaler, P. G. Kevrekidis, and D. J. Frantzeskakis, Phys. Rev. A **72**, 023609 (2005).

[42] L. A. Toikka, J. Hietarinta, and K.-A. Suominen, J. Phys. A: Math. Theor. **45**, 485203 (2012).

[43] A. M. Kamchatnov and S. V. Korneev, Phys. Lett. A **374**, 4625 (2010).

[44] L. D. Carr and C. W. Clark, Phys. Rev. A **74**, 043613 (2006).

[45] W. Wang, P. G. Kevrekidis, R. Carretero-González, and D. J. Frantzeskakis, Phys. Rev. A **93**, 023630 (2016).

[46] N. S. Ginsberg, J. Brand, and L. V. Hau, Phys. Rev. Lett. **94**, 040403 (2005).

[47] N. Akhmediev and A. Ankiewicz, Phys. Rev. A **47**, 3213 (1993).

[48] Yu. S. Kivshar and W. Królikowski, Opt. Commun. **114**, 353 (1995).

[49] M. P. Coles, D. E. Pelinovsky, and P. G. Kevrekidis, Nonlinearity **23**, 1753 (2010).

[50] G. L. Alfimov and D. A. Zezyulin, Nonlinearity **20**, 2075 (2007).

[51] C. Menotti and S. Stringari, Phys. Rev. A **66**, 043610 (2002).

[52] T. Busch and J. R. Anglin, Phys. Rev. Lett. **84**, 2298 (2000).

[53] A. S. Bradley and B. P. Anderson, Phys. Rev. X **2**, 041001 (2012).

[54] M. T. Reeves, T. P. Billam, B. P. Anderson, and A. S. Bradley, Phys. Rev. A **89**, 053631 (2014).

[55] T. P. Billam, M. T. Reeves, B. P. Anderson, and A. S. Bradley, Phys. Rev. Lett. **112**, 145301 (2014).

[56] T. Simula, M. J. Davis, and K. Helmerson, Phys. Rev. Lett. **113**, 165302 (2014).

[57] Yu. S. Kivshar, A. Nepomnyashchy, V. Tikhonenko, J. Christou, and B. Luther-Davies, Opt. Lett. **25**, 123 (2000).

[58] D. Neshev, A. Nepomnyashchy, and Yu. S. Kivshar, Phys. Rev. Lett. **87**, 043901 (2001).

[59] V. P. Ruban, JETP Lett. **106**, 223 (2017).

[60] C. Ticknor, W. Wang, and P. G. Kevrekidis, Phys. Rev. A **98**, 033609 (2018).

[61] M. Konstantinov, Phys. Fluids **6**, 1752 (1994).

[62] R. M. Caplan, J. D. Talley, R. Carretero-González, and P. G. Kevrekidis, Phys. Fluids **26**, 097101 (2014).

[63] W. Wang, R. N. Bisset, C. Ticknor, R. Carretero-González, D. J. Frantzeskakis, L. A. Collins, and P. G. Kevrekidis, Phys. Rev. A **95**, 043638 (2017).